ACCSCIENCE PUBLISHING

Materials Science in Additive Manufacturing

ORIGINAL RESEARCH ARTICLE

Effect of rotational speed on the microstructure and corrosion resistance of 2219 aluminum alloy manufactured by additive friction stir deposition

Zikang Wang[1,2,3], Hongchang Qian[1,3]*, Qian Qiao[4], Min Zhou[5], Zhixiong Zhu[6], Yongyong Lin[6], Dawei Guo[4], Dawei Zhang[1,2,3]*, Chi Tat Kwok[5], and Lap Mou Tam[4,5]

[1]National Materials Corrosion and Protection Data Center, Institute for Advanced Materials and Technology, University of Science and Technology Beijing, Beijing, China

[2]School of Advanced Materials Innovation, University of Science and Technology Beijing, Beijing, China

[3]Belt and Road Initiative Southeast Asia Network for Corrosion and Protection (MOE), Shunde Innovation School, University of Science and Technology Beijing, Foshan, Guangdong, China

[4]IDQ Science and Technology Development (Hengqin, Guangdong) Co., Ltd., Zhuhai, Guangdong, China

[5]Department of Electromechanical Engineering, Faculty of Science and Technology, University of Macau, Macao SAR, China

[6]Aerospace Engineering Equipment (Suzhou) Co., Ltd., Suzhou, Jiangsu, China

***Corresponding authors:**
Hongchang Qian
(qianhc@ustb.edu.cn)
Dawei Zhang
(dzhang@ustb.edu.cn)

Citation: Wang Z, Qian H, Qiao Q, *et al*. Effect of rotational speed on the microstructure and corrosion resistance of 2219 aluminum alloy manufactured by additive friction stir deposition. *Mater Sci Add Manuf*. 2026;5(2):025420100. doi: 10.36922/MSAM025420100

Received: October 17, 2025

Revised: November 10, 2025

Accepted: November 19, 2025

Published Online: January 12, 2026

Abstract

The 2219 aluminum alloy is widely utilized in critical structural components owing to its superior overall performance, while additive friction stir deposition (AFSD) exhibits potential for large-scale manufacturing. However, research on the corrosion behavior of AFSD-fabricated materials remains limited, and the influence of process parameters on corrosion mechanisms requires further exploration. This study compares the microstructure and corrosion resistance of different deposition layers in 2219 aluminum alloy fabricated by AFSD at rotational speeds of 400 rpm and 700 rpm. Higher rotational speed (700 rpm) generated greater thermal input and plastic deformation, promoting dynamic recrystallization and leading to larger grain sizes (bottom layer: 3.40 μm [400 rpm] vs. 3.83 μm [700 rpm]; top layer: 2.50 μm [400 rpm] vs. 3.01 μm [700 rpm]) and increased high-angle grain boundaries (bottom layer: 71.5% [400 rpm] vs. 75.2% [700 rpm], top layer: 57.3% [400 rpm] vs. 63.0% [700 rpm]). The bottom layer, experiencing more thermal cycles, showed further grain growth and resulted in larger grain sizes. At 700 rpm, greater precipitation of the Al_2Cu phase increased the number of micro-galvanic couples between precipitates and the aluminum matrix, accelerating corrosion. Conversely, greater thermal input in the bottom layer promoted Cu dissolution and reduced precipitate formation, improving corrosion resistance compared to the top layer. Consequently, the bottom layer processed at 400 rpm exhibited the optimal corrosion resistance, with the highest R_{ct} value of 4.17×10^3 Ω·cm^2. As the rotational speed decreased, the corrosion resistance was enhanced.

Keywords: Rotational speed; Microstructure; Corrosion; Additive friction stir deposition

1. Introduction

Aluminum and its alloys occupy a critical position in various industrial sectors.[1-3] Among them, the 2219 aluminum alloy exhibits high specific strength, excellent fatigue strength, and superior machinability, making it widely used in the aerospace industry and large-scale equipment manufacturing.[4-7] As science and industry advance, the specification requirements for large-scale 2219 aluminum alloy components have become increasingly stringent, accompanied by a corresponding rise in the complexity of their manufacturing processes.[8,9] Traditional large forgings are typically fabricated through conventional techniques, such as casting and forging, with their quality predominantly determined by the inherent properties of the ingots.[10] However, large aluminum ingots prepared through these methods often contain internal defects such as segregation and porosity.[11,12] These defects can exert adverse effects on the quality of forgings during subsequent processing and ultimately shorten their service life. Furthermore, conventional techniques are generally plagued by challenges such as difficulties in manufacturing complex components and low material utilization. In contrast, additive manufacturing, as an emerging fabrication technology, enables the integrated formation of complex components due to its high flexibility in production.[13-15] This renders it a promising solution to the aforementioned issues encountered in traditional methods.

Additive friction stir deposition (AFSD), as a novel solid-state additive manufacturing technology, shows excellent application prospects in producing large-scale (meter-sized) metal structures and fabricating dissimilar metals. The principle of AFSD is based on friction stir welding technology,[16] built on the fundamentals of severe plastic deformation during hot working. It utilizes the principle of solid-state friction extrusion and plastic deformation to achieve metal joining and forming, possessing the potential to fabricate fully dense components free from solidification-related metallurgical defects.[17,18] The process involves a rotating tool driving a consumable feedstock rod under high axial pressure. On contacting the substrate, intense friction creates a plastic deformation flow, forming a strong metallurgical bond with the underlying material. Layer-by-layer deposition along predefined 3D paths enables additive manufacturing. Compared to traditional fusion-based additive manufacturing methods, AFSD offers significant advantages in producing large-scale components, forming defect-free uniform microstructures, and reducing manufacturing cycle time and cost.[19-21]

At present, research on 2219 aluminum alloys fabricated through AFSD has primarily focused on their microstructure and mechanical properties, with attention paid to ultimate tensile strength (UTS), yield strength, and elongation. Table 1 summarizes the process parameters and tensile performance from relevant studies.[22-24] However, studies on their corrosion resistance remain relatively scarce. In our previous investigation into the corrosion behavior of AFSD-2219 aluminum alloy, we observed a degradation in corrosion resistance compared to the feedstock.[25] This phenomenon is attributed to the significant increase in precipitate phases induced by the AFSD process, leading to a higher density of micro-galvanic couples formed between the precipitates and the aluminum matrix. Consequently, both pitting corrosion and intergranular corrosion were exacerbated in the AFSD-2219 alloy.

The process parameters of AFSD technology, such as travel speed, rotational speed, and feed rate, play a crucial role in determining the performance of fabricated parts.[26] Variations in these parameters result in different levels of force, torque, and heat input, ultimately affecting the quality and mechanical properties of the products. Among these, rotational speed has received significant attention from researchers as a critical influencing factor in AFSD processes. For example, Qiao *et al*.[27] investigated

Table 1. Process parameters and tensile properties of the reported AFSD-2219 aluminum alloy

Material	Rotational speed (rpm)	Travel speed (mm/min)	Feed rate (mm/min)	UTS (MPa)	YS (MPa)	Elongation (%)	References
AFSD-2219 (T87-B)	200	101.6	88.9	202	86	35	22
AFSD-2219 (T87-L)	200	101.6	88.9	206	84	38	22
AFSD-2219 (casting-L)	400	150	100	212.3	124.1	29.2	23
AFSD-2219 (T4-L)	400	150	100	246.5	140.4	29.6	23
AFSD-2219 (T87-L)	400	150	100	257.7	147.2	28.4	23
AFSD-2219 (T851-L-T)	-	-	-	390	159	25	24
AFSD-2219 (T851-L-M)	-	-	-	364	140	27	24
AFSD-2219 (T851-L-B)	-	-	-	335	125	28	24

Abbreviations: AFSD: Additive friction stir deposition; UTS: Ultimate tensile strength; YS: Yield strength.

the microstructure and mechanical response in AFSD-6061 aluminum alloy at three rotations and found that its deformation textures showed obvious differences under different rotational speeds. In addition, heat input scaled with rotational speed, leading to an enlargement of grains. When the rotational speed was 550 rpm, the AFSD-6061 aluminum alloy exhibited the highest average microhardness due to the dislocation strengthening effect, while the highest yield strength (87.8 MPa) and UTS (147.2 MPa) were obtained at 450 rpm. Likewise, Chen *et al.*[28] investigated the effects of rotational speed and feed rate on the microstructural evolution and mechanical performance of AFSD-6061 aluminum alloy. The results showed that the AFSD process reduced the tensile strength of the alloy, while the grain size and tensile strength were increased with feed rate and rotational speed. In contrast, the reduction of area was negatively correlated with them. Thus, rotational speed exerts a pronounced influence on both microstructural evolution and properties of materials produced by AFSD. Specifically, rotational speed variations affect dynamic recrystallization (DRX) by modulating the generation of frictional heat and the extent of plastic deformation. In addition, differences in thermal exposure time resulting from varying rotational speeds influence the distribution and quantity of precipitated phases, thereby impacting mechanical properties and corrosion resistance.

In this work, a systematic study was carried out on the microstructure of the top and bottom layers of multi-layer as-deposited AFSD-2219 aluminum alloy formed at different rotational speeds and their corrosion behavior in 3.5 wt% NaCl solution. The AFSD process was monitored *in situ* in real time to analyze changes in force and torque. The microstructure and phase composition of the AFSD-fabricated parts were characterized, and the dynamic evolution law of the corrosion process of various samples was analyzed through immersion experiments. The corrosion morphology of each sample after immersion was then observed. Compared to previous studies,[22-25] this work investigated the effects of rotational speed on the corrosion behavior of AFSD-2219 aluminum alloy. It provides a novel insight that adjusting process parameters can serve as an alternative to post-processing heat treatment to enhance the corrosion resistance of alloy components.

2. Materials and methods

2.1. Materials

In this study, 2219 aluminum alloy rods in the T6 temper were used as the feedstock, with dimensions of 10 mm × 10 mm × 400 mm. The T6 temper represents a peak strength condition and has broad representativeness in aerospace structures. In addition, the substrates with dimensions of 300 mm × 80 mm × 8 mm were fabricated from a 2219 aluminum alloy sheet, which also underwent T6 heat treatment. A thicker substrate can effectively inhibit angular distortion, warpage, and waviness, and the 2219 aluminum alloy substrate in the T6 temper maintains consistency with the raw material rod to facilitate metallurgical bonding. The elemental composition of the feedstock is presented in Table 2.

2.2. AFSD fabrication

Samples were fabricated on an MSAM-B20×15 solid-state additive system (Aerospace Engineering Equipment [Suzhou] Co., Ltd., China). The schematic diagram of the preparation process is shown in Figure 1. For sample fabrication, two distinct spindle rotational speeds, 400 rpm and 700 rpm, were employed, representing conditions of low and high thermal input within the defect-free processing window, respectively. Meanwhile, the travel speed (V_t) and feed rate (V_f) were consistently set at 70 mm/min and 28.67 mm/min, respectively, to isolate the effect of the rotational speed. The procedure parameters (temperature, force, and torque) were monitored using an *in situ* process-monitoring kit. The deposition length of a single layer was 100 mm, and the layer thickness was 1.5 mm. Subsequently, 10 mm × 10 mm × 3 mm samples were taken from the top and bottom of the deposited material, with the 10 mm × 10 mm surface aligned parallel to the longitudinal direction (LD) of deposition. The specific sampling locations are illustrated in Figure 1. In this paper, the top and bottom portions of samples deposited at 400 rpm are referred to as the 400-top and 400-bottom samples, respectively, while those at 700 rpm are referred to as the 700-top and 700-bottom samples, respectively (Table 3).

Table 2. Elemental composition of the 2219 aluminum alloy feedstock

Element	Composition (wt%)
Al	92.585
Cu	6.487
Fe	0.128
Mn	0.266
Si	0.042
Mg	0.020
V	0.092
Zn	0.066
Zr	0.172
Ti	0.038

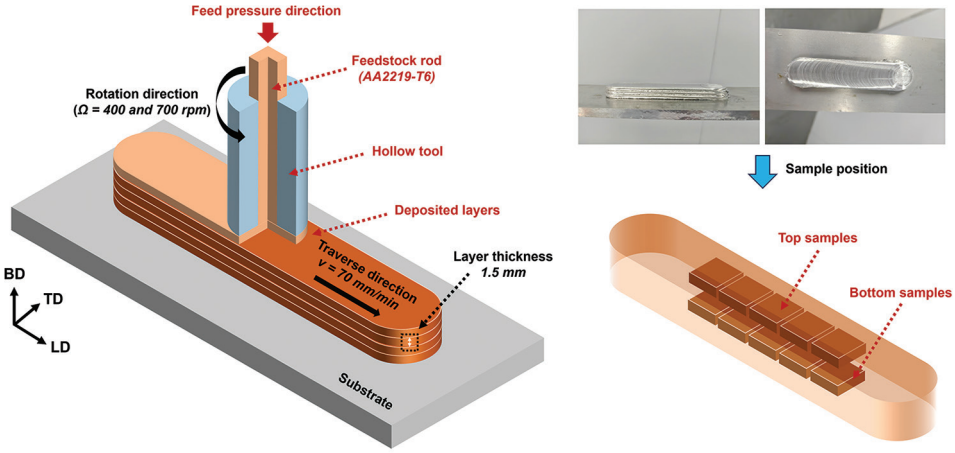

Figure 1. Schematic of the additive friction stir deposition process and the specific sampling locations
Abbreviations: BD: Building direction; LD: Longitudinal direction; TD: Transverse direction

Table 3. Production parameters of the four samples

Sample	Rotational speed (rpm)	Travel speed (mm/min)	Feed rate (mm/min)	Layer thickness (mm)	Location
400-bottom	400	70	28.67	1.5	Bottom layer
400-top	400	70	28.67	1.5	Top layer
700-bottom	700	70	28.67	1.5	Bottom layer
700-top	700	70	28.67	1.5	Top layer

2.3. Microstructure and composition characterization

The surface morphologies of the samples were characterized using scanning electron microscopy (SEM; Sigma 560, Zeiss, Germany) with an energy dispersive spectrometer (EDS; Ultim Max, Oxford Instruments, United Kingdom [UK]). Quantitative analysis of the proportion of the intermetallic phase was performed using the Image J software (National Institutes of Health, United States [US]). The microstructures of the four samples were characterized through electron backscatter diffraction (EBSD; NordlysNano, Oxford Instruments, UK) with a step size of 0.25 μm.

Before SEM observation and EBSD testing, the samples were sequentially ground using silicon carbide paper (400#, 800#, 1200#, 2000#, and 3000#), followed by mechanical polishing with a 1.5 μm diamond suspension and ultrasonically cleaning in deionized water and anhydrous ethanol. Subsequently, the samples underwent ion polishing using a triple ion beam cutting instrument (EM TIC 3×, Leica Microsystems, Germany) to eliminate surface stress (operating conditions: voltage of 8 kV, current of 3 mA). X-ray diffraction (XRD; D8 Advance, Bruker Corporation, Germany) was employed for phase analysis of the samples. The measurements were conducted with a scanning speed of 6°/min. The phase composition was determined using the Jade 6.0 software (Materials Data, Inc., US).

2.4. Electrochemical tests

A three-electrode configuration was adopted for the electrochemical experiments. The alloy samples served as the working electrode, a platinum sheet (20 mm × 20 mm) acted as the counter electrode, and a saturated calomel electrode (SCE) as the reference electrode. All tests were conducted at room temperature in the 3.5 wt% NaCl solutions using an electrochemical workstation (Reference 600 Plus, Gamry Instruments, Inc., US). Before testing, Cu wires were welded onto the backside of the working electrode and insulated with epoxy resin, leaving an exposed working surface area of 10 mm × 10 mm. To ensure the stability of the three-electrode system, the open-circuit potential was measured for 900 s. Following this, electrochemical impedance spectroscopy (EIS) measurements were carried out over a frequency range of 100 kHz to 10 mHz with a sinusoidal perturbation amplitude of 10 mV. The EIS data were analyzed and fitted using ZSimpWin software (Version 3.60, Echem Software, US). Three parallel samples were adopted to guarantee the reliability and accuracy of the experimental results.

2.5. Corrosion morphology characterization

Immersion tests were carried out in 3.5 wt% NaCl at ambient temperature (25°C). The samples were immersed for 1 d and 7 d. The corrosion products were removed using a nitric acid solution. The surface morphologies of the samples before and after corrosion product removal were

characterized using an SEM. The elemental distribution of the corrosion products was analyzed via EDS. In addition, the chemical composition of the corrosion products was determined using X-ray photoelectron spectroscopy (XPS; ESCALAB 250Xi, Thermo Fisher Scientific, US). After removal of corrosion products, the three-dimensional surface morphology was characterized by confocal laser scanning microscopy (CLSM; VK-X250K, Keyence Corporation, Japan).

3. Results and discussion

3.1. *In situ* procedure parameter during AFSD

Figure 2 illustrates the variations of spindle pressure (F_{spi}), spindle torque (M_{spi}), and spindle temperature over time during the AFSD manufacturing process at rotational speeds of 400 rpm and 700 rpm. F_{spi}, M_{spi}, and spindle temperature are closely associated with the dynamic deformation behavior of the feedstock rod during AFSD and serve as critical factors influencing heat input, material plasticity, metallurgical bonding quality, and final mechanical properties.[29,30] In the initial stage of AFSD (0–140 s), the hollow rotation tool removed oxides and impurities from the substrate surface, resulting in minor fluctuations in F_{spi}, M_{spi}, and spindle temperature. During the stable deposition phase (140–760 s), the rotation tool traversed along the LD direction at a preset rotational speed and movement velocity. Under the combined effects of top forging force and high-temperature friction, the feedstock rod softened and underwent large plastic deformation, forming a flow that deposited onto the substrate. Consequently, the F_{spi}, M_{spi}, and spindle temperature exhibited a sharp increase followed by relative stability. Notably, at certain points during this phase, there were transient decreases in F_{spi}, M_{spi}, and spindle temperature, attributed to the lifting of the rotation tool following the completion of single-layer deposition. In the final sedimentation stage (760–830 s), the rotation tool fully disengaged from the sediment, causing the F_{spi}, M_{spi}, and spindle temperature to plummet sharply to zero.

At 400 rpm and 700 rpm, the spindle temperatures were recorded at 460.64 ± 27.89°C and 503.27 ± 33.94°C, respectively. The higher rotational speed clearly resulted in a higher temperature, and such differences in thermal conditions distinctly influenced the material during the AFSD process. This effect not only impacted F_{spi} and M_{spi} but also altered the microstructure and properties of the as-deposited alloy. The F_{spi} values at 400 rpm

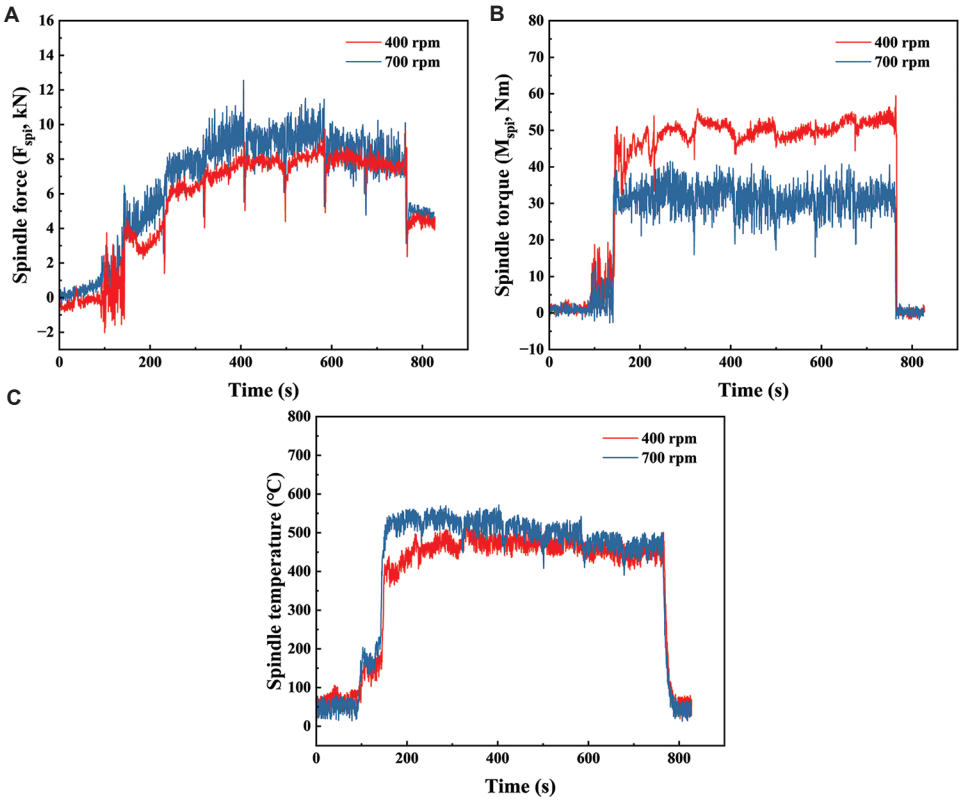

Figure 2. The variation of (A) spindle force (F_{spi}), (B) spindle torque (M_{spi}), and (C) spindle temperature over time during the additive friction stir deposition manufacturing process of 2219 aluminum alloy

and 700 rpm were 6.91 ± 1.64 kN and 8.03 ± 1.69 kN, respectively. The feed rate remained constant at both speeds, suggesting that the variation in F_{spi} was primarily attributed to the difference in rotational speeds. The higher rotational speed generated a higher temperature environment, which enhanced the thermal expansion of the feedstock rod. This resulted in an increased force exerted by the feedstock rod on the spindle shoulder at the exit of the hollow rotation tool, thereby elevating the F_{spi}. Conversely, as the rotational speed increased from 400 rpm to 700 rpm, M_{spi} decreased from 49.57 ± 3.27 Nm to 31.48 ± 3.94 Nm. M_{spi} was closely associated with the yield strength and flow stress of the feedstock.[31] At 700 rpm, the elevated environmental temperature induced by the higher rotational speed intensified the softening degree of the feedstock rod, reducing its resistance to plastic deformation and flow stress, ultimately leading to a reduction in the M_{spi}.[32]

3.2. Microstructure and composition evolution

The SEM images in Figure 3 illustrate the surface morphologies of the 400-bottom, 400-top, 700-bottom, and 700-top samples. It was evident that precipitated phase particles were uniformly dispersed within the aluminum alloy matrix across all samples. As can be seen in high-magnification SEM images, the average size of these small precipitated phase particles was approximately 1 μm. However, some large particles were still observed. In general, the top-layer samples (400-top and 700-top) contained a greater number of large particles compared to the bottom-layer samples (400-bottom and 700-bottom). Specifically, the size of the large particles in the 700-top sample approached 15 μm. The EDS elemental mapping results (Figure 3A3-D3) revealed that the precipitated phase particles primarily consist of aluminum and Cu elements, as detailed in Table 4. The atomic percentage of Cu ranged approximately 3%, with the highest value reaching 4.23% in the 700-top sample, indicating that more Cu precipitated from the solid solution of the 700-top sample to form precipitate phase particles.

Figure 4 shows the coverage rates of the precipitated phase particles for the 400-bottom, 400-top, 700-bottom, and 700-top samples, with respective coverage rates of 10.99%, 16.91%, 12.45%, and 18.34%. Compared to 400 rpm, the coverage rate of the precipitated phase at 700 rpm slightly increased. The more intense plastic deformation generated at the higher rotational speed caused greater fragmentation of the secondary phases and introduced a higher density of dislocations. As a

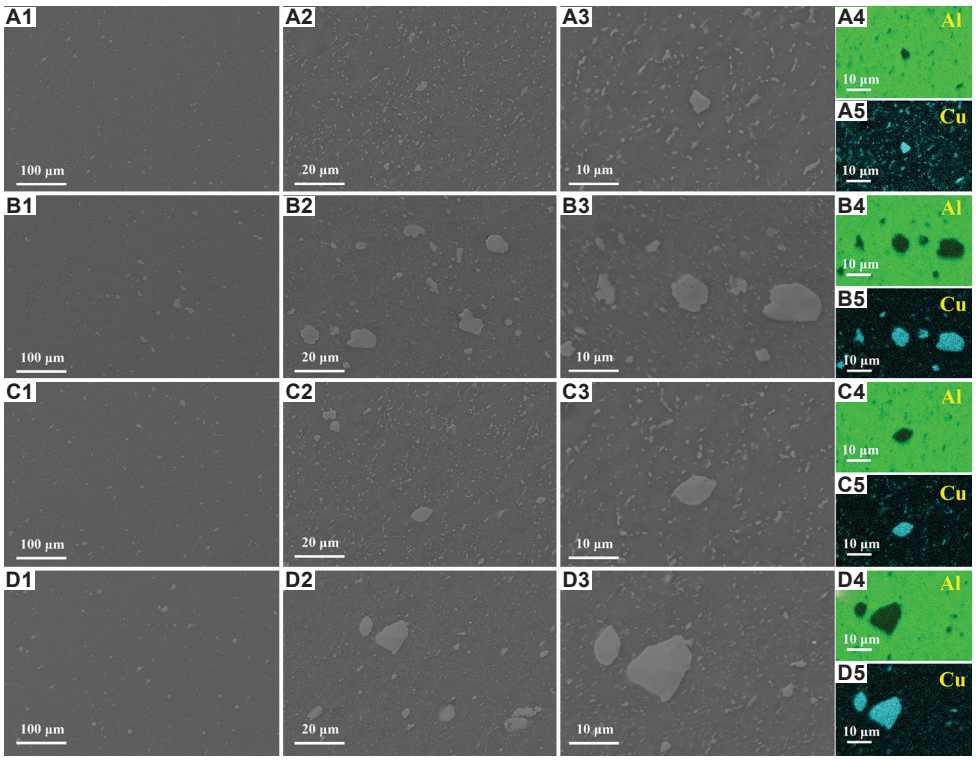

Figure 3. Surface scanning electron microscopy morphologies and energy dispersive spectroscopy mapping of (A_1-A_5) 400-bottom sample, (B_1-B_5) 400-top sample, (C_1-C_5) 700-bottom sample, and (D_1-D_5) 700-top sample. (A_1-D_1) 100 μm; (A_2-D_2) 20 μm, (A_3-D_3, A_4-D_4, A_5-D_5) 10 μm; magnifications: (A_1-D_1) ×200; (A_2-D_2) ×1000, (A_3-D_3, A_4-D_4, A_5-D_5) ×2000

Table 4. Elemental atomic percentages from energy dispersive spectroscopy (at%)

Sample	Al	Cu	Fe	Mn	V	Ti	Zr
400-bottom	96.84	2.83	0.06	0.16	0.06	0.00	0.05
400-top	96.44	3.20	0.06	0.15	0.06	0.04	0.04
700-bottom	96.75	2.94	0.06	0.14	0.05	0.02	0.04
700-top	95.41	4.23	0.04	0.16	0.07	0.04	0.06

consequence, these deformation-induced defects provided a substantially larger number of nucleation sites for precipitate formation, thereby increasing the coverage rate of the precipitate.[33-35] However, the differences in coverage rates were minor, suggesting that rotational speed had a limited influence on the coverage rate of the precipitated phase particles. In contrast, under identical rotational speed, the coverage rate at the top layer (400-top and 700-top) was markedly higher than at the bottom layer (400-bottom and 700-bottom). Specifically, the coverage rate of the 400-top sample exceeded that of the 400-bottom sample by 53.87%, while the coverage rate of the 700-top sample surpassed that of the 700-bottom sample by 47.31%. This was because the bottom samples experienced multiple high-temperature thermal cycles during the AFSD process, which functioned as multiple solid solution treatments, causing more Cu to return to the aluminum solid solution.

The compositional analysis of the four samples was further conducted using XRD. The XRD patterns of all samples are shown in Figure 5. The diffraction peaks at 21°, 42°, and 48° corresponded to the (110), (112), and (202) crystal planes of the Al_2Cu phase,[36] respectively, while the peaks at 38°, 44°, 65°, 78°, and 82° were attributed to the (111), (200), (220), (311), and (222) crystal planes of the aluminum phase, respectively. The diffraction peaks attributable to Al_2Cu were much weaker than those of Al. Together with the EDS elemental analysis, this identifies the precipitates as Al_2Cu.

Images related to the EBSD of all samples are presented in Figure 6. In addition, grain sizes and misorientation distributions are illustrated in Figure 7. During large plastic deformation in AFSD, the microstructure evolution of the material is often accompanied by dynamic recovery and DRX, resulting in the formation of fine equiaxed grain structures.[37] It can be confirmed by the inverse pole figure images in Figure 6A-H. The average grain sizes for the 400-bottom, 400-top, 700-bottom, and 700-top samples were 3.40 μm, 2.50 μm, 3.83 μm, and 3.01 μm, respectively. The grain sizes at 700 rpm were slightly larger than those at 400 rpm. This could be attributed to that a higher rotational speed resulted in greater heat input and

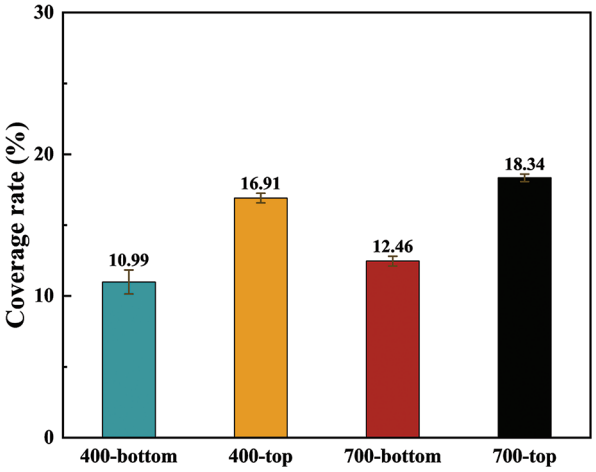

Figure 4. The coverage rates of precipitation phase particles of the 400-bottom, 400-top, 700-bottom, and 700-top samples

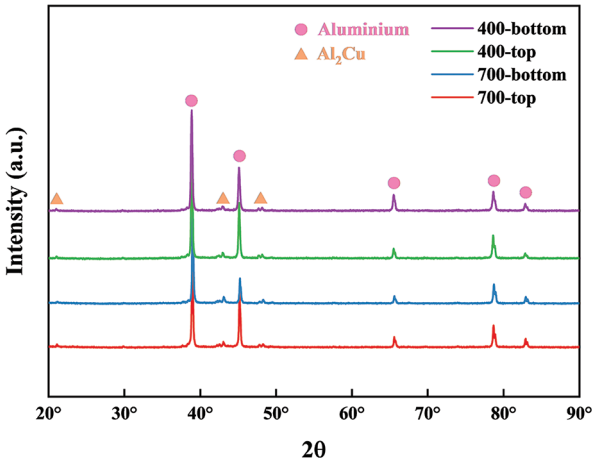

Figure 5. X-ray diffraction patterns of the 400-bottom, 400-top, 700-bottom, and 700-top samples

plastic deformation, both of which lowered the threshold for the occurrence of the continuous DRX process. This enhanced the grain boundary migration ability and facilitated grain growth.[38] At the same rotational speed, the grain sizes of the top-layer samples (400-top and 700-top) were smaller than those of the bottom-layer samples (400-bottom and 700-bottom). This was because the bottom-layer samples experienced multiple thermal cycles, leading to increased heat input that further stimulated grain growth during DRX.

During the AFSD processing, the subgrain boundaries of the 2219 aluminum alloy continuously absorb dislocations, leading to a gradual increase in the crystallographic misorientation between adjacent grains. The process entails progressive conversion of low-angle grain boundaries

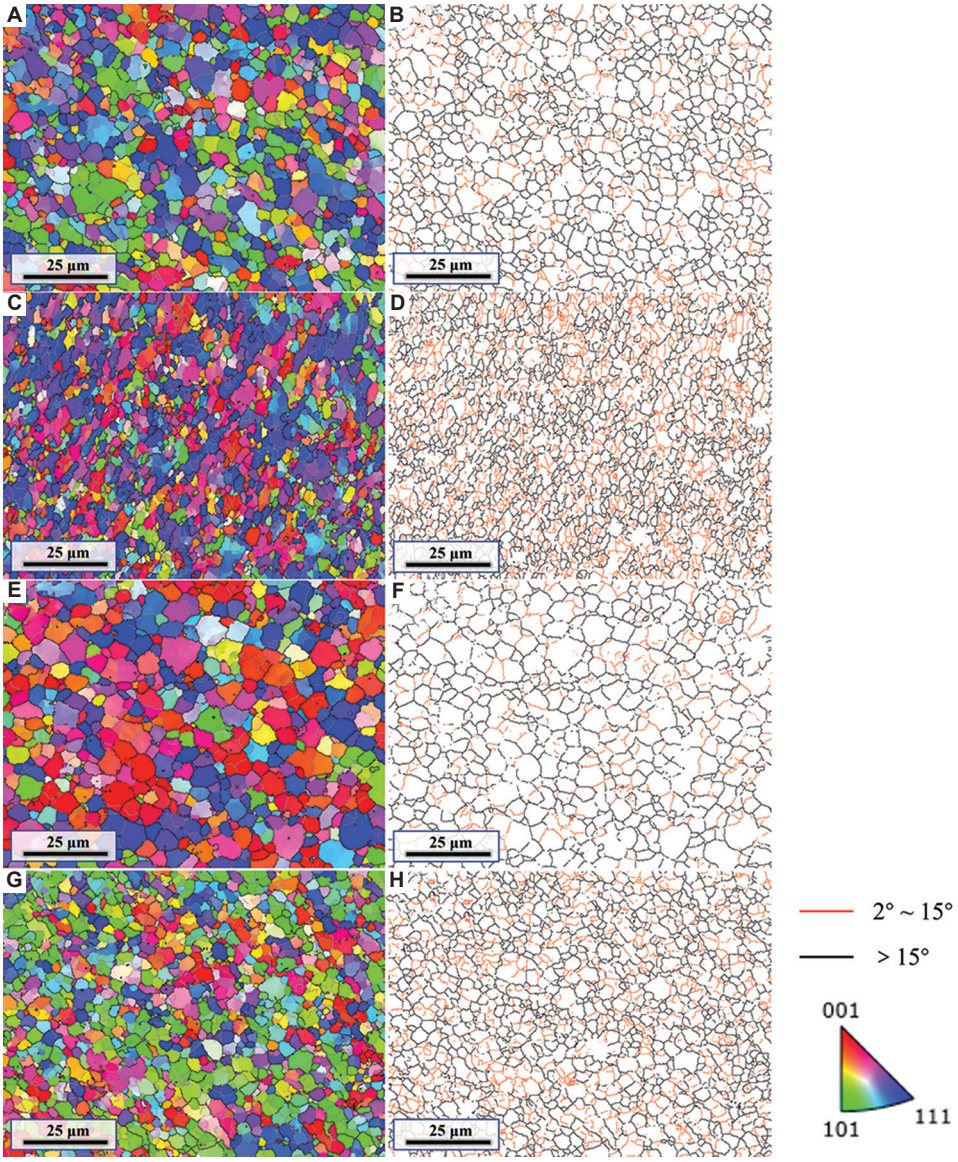

Figure 6. Inverse pole figure images and grain boundary maps of the (A and B) 400-bottom, (C and D) 400-top, (E and F) 700-bottom, and (G and H) 700-top samples. Scale bars: 25 μm; magnifications: 1000×

(LAGBs) to high-angle grain boundaries (HAGBs), culminating in the formation of recrystallized grains.[39,40] Thus, the distribution of HAGBs and LAGBs serves as an indicator of the degree of grain recrystallization. The proportions of HAGBs in the 400-bottom, 400-top, 700-bottom, and 700-top samples were 71.5%, 57.3%, 75.2%, and 63.0%, respectively, while the proportions of LAGBs were 28.5%, 42.7%, 24.8%, and 37.0%, respectively. It is evident that the proportions of HAGBs in the bottom samples were markedly higher than those in the top samples. The pinning effect of precipitated phase particles restricts dislocation movement, thereby inhibiting the transformation of LAGBs into HAGBs. Since the top samples contained more precipitated phase particles, this resulted in a higher proportion of HAGBs. In addition, the proportions of HAGBs in the samples processed at 700 rpm were slightly higher than those processed at 400 rpm. This difference was ascribed to the greater accumulation of deformation-stored energy in the alloy processed at 700 rpm, which provided a stronger driving force for dislocation movement.[41] Consequently, the 700-bottom sample exhibited the highest degree of recrystallization, whereas the 400-top sample demonstrated the lowest degree of recrystallization, with a considerable number of deformed grains and subgrains inside. These results suggest that the large plastic deformation induced by high rotational

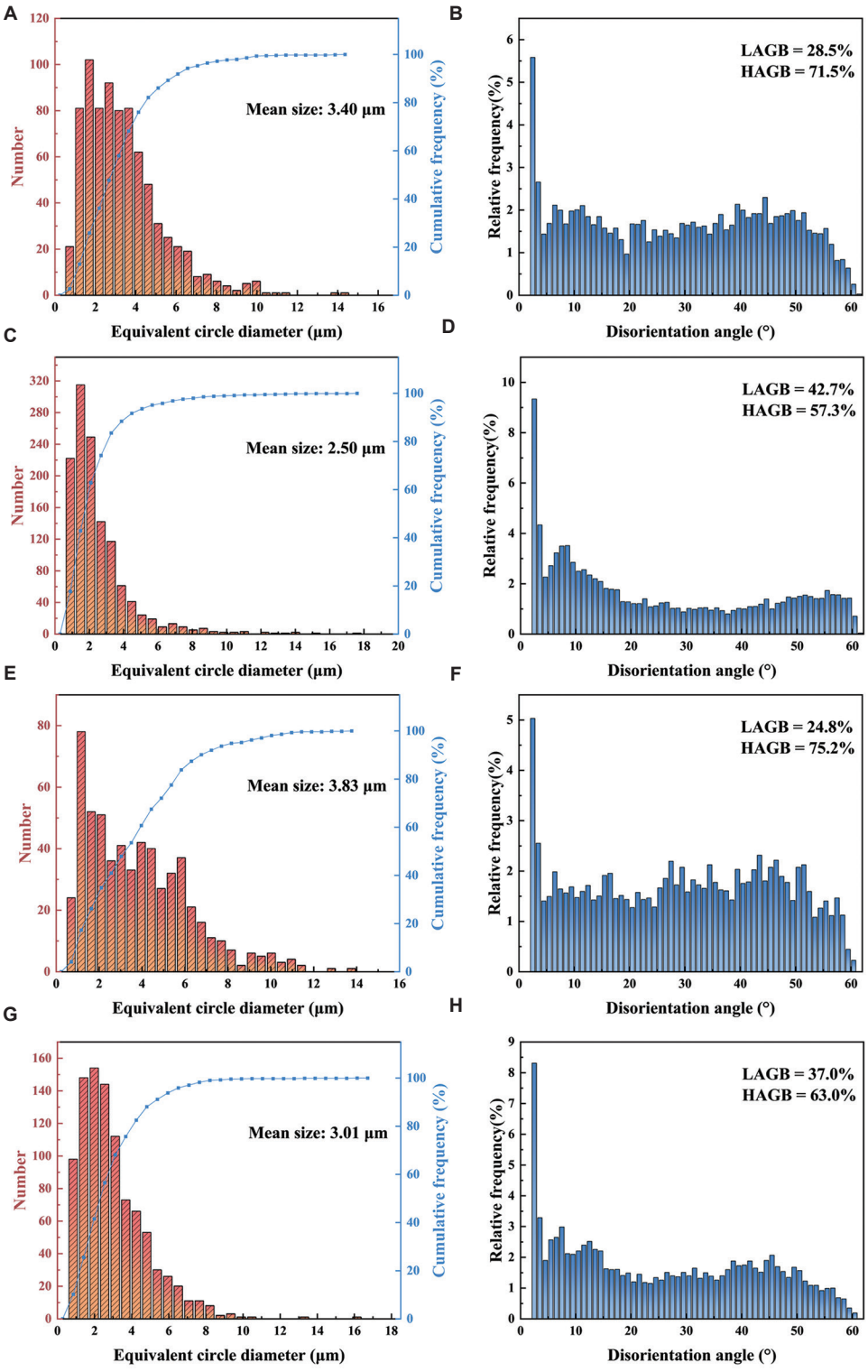

Figure 7. Grain sizes and misorientation distributions of the (A and B) 400-bottom, (C and D) 400-top, (E and F) 700-bottom, and (G and H) 700-top samples
Abbreviations: HAGB: High-angle grain boundary; LAGB: Low-angle grain boundary

speed and the thermal cycling effect during multi-layer deposition effectively facilitated the DRX process.

The grain orientation spread (GOS) conditions of the samples were analyzed, and the results are illustrated in Figures 8 and 9. High GOS values indicate a substantial dislocation density and severe lattice distortion within the grains, whereas low GOS values suggest a more uniform strain distribution and reduced dislocation density.[42,43]

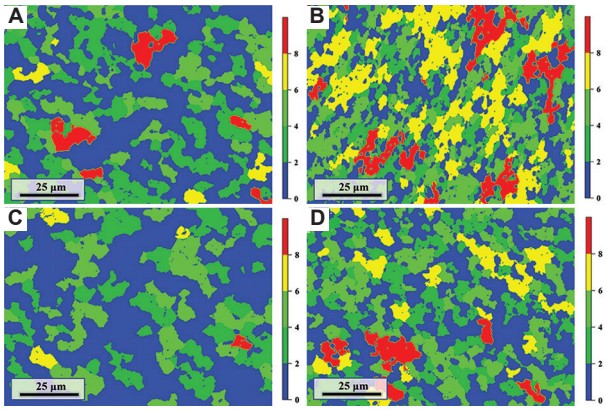

Figure 8. The grain orientation spread images of the (A) 400-bottom, (B) 400-top, (C) 700-bottom, and (D) 700-top samples. Scale bars: 25 μm; magnifications: 1000×

The average GOS values for the 400-bottom, 400-top, 700-bottom, and 700-top samples were 2.54°, 4.26°, 2.08°, and 3.19°, respectively. These results align with the distribution trend of HAGBs. The low GOS values observed in the 400-bottom and 700-bottom samples suggest that the thermal cycling effect during multi-layer deposition effectively promoted recrystallization. Conversely, the high GOS values of the 400-top and 700-top samples, indicative of regions with elevated dislocation densities, were likely to act as critical sites for corrosion initiation.[44]

Based on real-time monitoring data during the AFSD process and microstructural characterization of the as-deposited samples, a correlation between the two datasets can be observed. By analyzing Figures 2 and 6, it can be concluded that the spindle temperature and F_{spi} are positively correlated with the grain size and the proportion of HAGBs in the as-deposited alloy. During AFSD, an increase in spindle speed enhances the relative motion between the material and the tool, resulting in higher heat input and more extensive plastic deformation. Consequently, both the spindle temperature and F_{spi} increase further. The combined effect of elevated temperature and F_{spi}, coupled with this stronger energy input, encourages grain growth

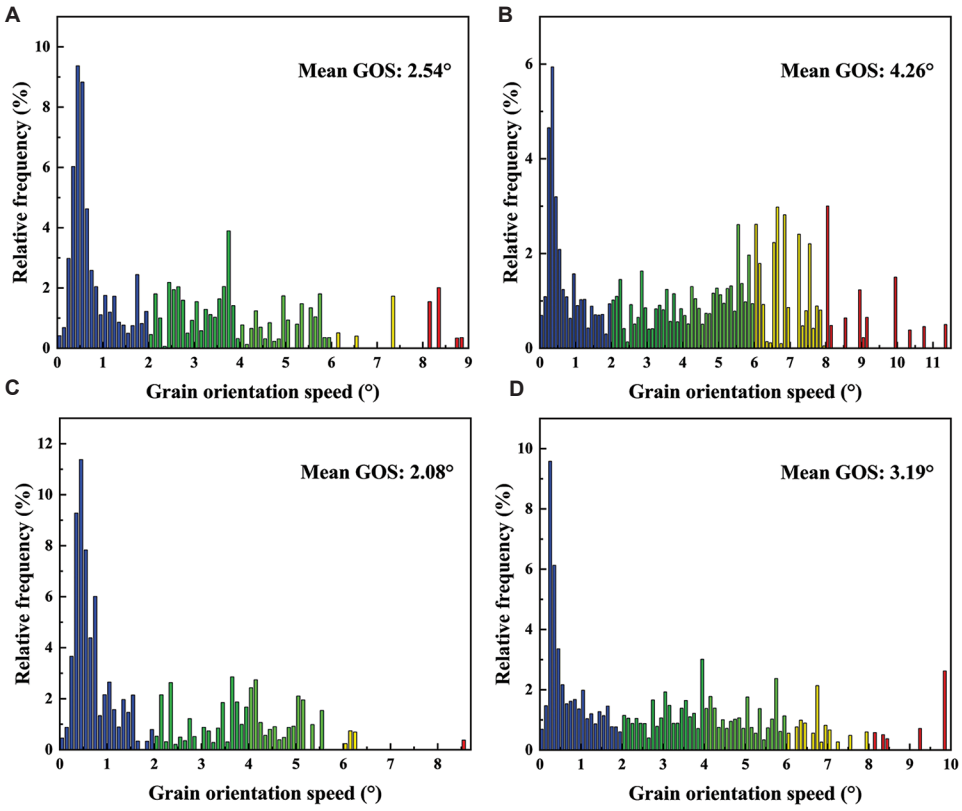

Figure 9. The grain orientation spread values of the (A) 400-bottom, (B) 400-top, (C) 700-bottom, and (D) 700-top samples

in the DRX process and simultaneously activates the formation of more HAGBs.

3.3. Electrochemical tests

The EIS plots of all samples after immersion in a 3.5 wt% NaCl solution for 0 h and 1 d are presented in Figure 10. At the outset of immersion (0 h), the Nyquist spectra for all four specimens (Figure 10A) displayed three features: Two capacitive loops at high and medium frequencies and an inductive loop at low frequency. The high-frequency capacitive loop was attributed to the interfacial reaction at the oxides/electrolyte interface, while the medium-frequency capacitive loop was associated with the charge transfer process occurring on the surface of the aluminum alloy substrate.[45,46] The low-frequency inductive loop was attributed to the relaxation phenomena on the aluminum alloy surface in the NaCl solution, which was related to the rapid failure of the oxide film on the sample surface.[47] After immersion for 1 d, the inductive loop in the low-frequency region disappeared in the Nyquist plot (Figure 10C). At this stage, the high-frequency capacitive loop reflected the interfacial reaction at the interface of oxides, corrosion products, and electrolyte, whereas the low-frequency capacitive arc represented the charge transfer process on the aluminum alloy substrate surface. Initially, the radius of the medium-frequency capacitive loop for the bottom-layer samples (400-bottom and 700-bottom) was markedly larger than that of the top-layer samples (400-top and 700-top), and the radius at 400 rpm was greater than that at 700 rpm. After 1 d of immersion, the radius of the capacitive arc related to charge transfer increased, potentially due to the accumulation of corrosion products on the sample surface.

Subsequently, the EIS spectra were fitted to the equivalent circuit models (EECs), as shown in Figure 11. Specifically, the EIS spectra at 0 h were fitted with the EEC shown in Figure 11A, while the EIS data at 1 d were fitted with the EEC depicted in Figure 11B. To account for the current inhomogeneity induced by the roughness of the working electrode surface and the capacitive dispersion effect,[48,49] a constant phase element (CPE) was employed to replace the ideal capacitor C, enabling a more accurate description of the EIS data.[50,51] In the EEC model, R_s denotes the solution resistance, Q_c and R_f represent the CPE and resistance associated with the mixed layer of oxides and corrosion products on the aluminum alloy surface, respectively, Q_{dl} and R_{ct} correspond to the electrical double-layer CPE and the charge-transfer resistance at the aluminum matrix surface, respectively, and Q_d and L signify the CPE and inductive resistance linked to the

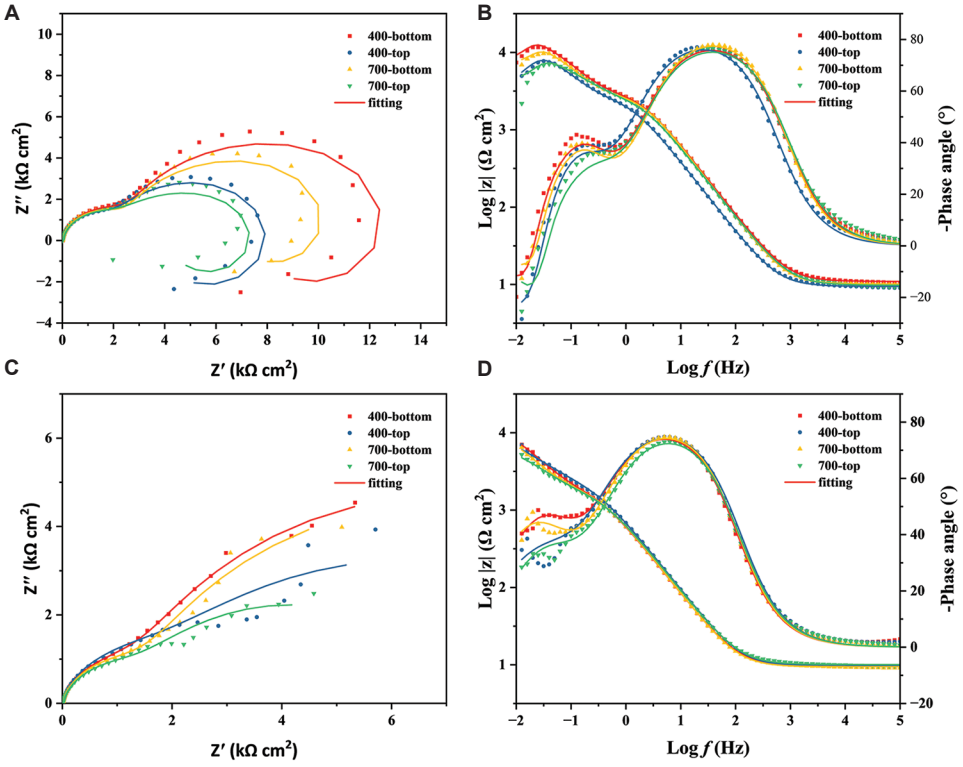

Figure 10. (A and C) Nyquist plots and (B and D) Bode plots of 400-bottom, 400-top, 700-bottom, and 700-top samples after immersion in 3.5 wt% NaCl solution for (A and B) 0 h and (C and D) 1 d

relaxation phenomenon caused by the rapid degradation of the passive film, respectively. The impedance of the CPE can be calculated using Equation (1):[52,53]

$$Z_{CPE} = Y_0^{-1} (j\omega)^{-n} \quad (1)$$

where Y_0 denotes the admittance magnitude of the CPE, j is the imaginary unit, ω is the angular frequency (rad/s), and n is the CPE exponent, typically between 0 and 1.

The parameters obtained from fitting the EIS spectra are summarized in Table 5. At the beginning of immersion and after 1 d, the R_{ct} values of the top-layer samples (400-top and 700-top) were consistently lower than those of the bottom-layer samples (400-bottom and 700-bottom). This indicates that the top-layer samples exhibited weaker corrosion resistance and a faster electrochemical reaction rate. In comparison with the R_{ct} values at 400 rpm, the R_{ct} values at 700 rpm decreased, suggesting that the electron transfer rates of the AFSD samples at 700 rpm were higher, thereby facilitating the electrochemical reaction. Notably, the R_{ct} values after 1 d were significantly higher than those at 0 h. This could be attributed to the formation of a corrosion product layer on the surface of the aluminum alloy, which hindered ion migration in the solution and indirectly suppressed the redox reaction at the interface. The electrochemical evaluation indicates a significant disparity in corrosion resistance among the samples. The maximum resistance was observed for the 400-bottom sample, while the minimum was recorded for the 700-top sample.

3.4. Corrosion morphology analysis

The SEM images of the corrosion products on the 400-bottom, 400-top, 700-bottom, and 700-top samples after immersion in a 3.5wt% NaCl solution for 1 d are presented in Figure 12. Local regions on the surfaces of the 400-bottom and 700-bottom samples exhibited accumulated corrosion products with dimensions ranging from 20 to 50 μm. By contrast, the corrosion products on the 400-top and 700-top samples were considerably more abundant. The clusters of corrosion products on the 400-top sample measured approximately 100 μm in size, whereas the surface of the 700-top sample was predominantly covered by corrosion products. These observations suggest that the top-layer samples (400-top and 700-top) experienced more severe corrosion, with the 700-top sample being the most severely corroded. High-

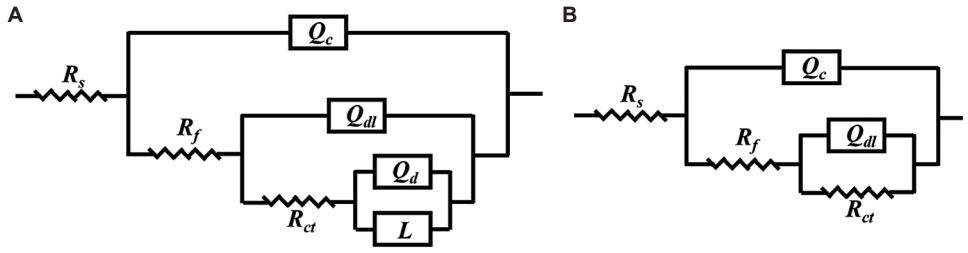

Figure 11. Schematic representations of the equivalent circuits used for fitting the experimental electrochemical impedance spectroscopy data. (A) Circuit incorporating an inductive element. (B) Circuit without inductance

Table 5. Electrochemical impedance spectroscopy data for the samples following 0 h and 1 d of exposure to 3.5 wt% NaCl solution

Parameter	0h				1d			
	400-bottom	400-top	700-bottom	700-top	400-bottom	400-top	700-bottom	700-top
R_s ($\Omega \cdot cm^2$)	10.93	9.42	10.12	9.76	9.78	9.67	9.42	10.07
$C_{eff,\ f}$ ($\times 10^{-5}$ $s^n/\Omega/cm^2$)	3.57	5.71	3.34	3.97	28.91	26.01	28.31	27.70
n	0.91	0.92	0.93	0.90	0.90	0.90	0.91	0.89
R_f ($\times 10^3$ $\Omega \cdot cm^2$)	3.55	1.92	3.19	3.18	2.32	2.64	2.18	2.00
$C_{eff,\ dl}$ ($\times 10^{-5}$ $s^n/\Omega/cm^2$)	21.38	22.74	25.58	23.41	95.50	95.15	126.20	133.30
n	1.00	0.20	0.99	1.00	0.85	0.72	0.84	0.80
R_{ct} ($\times 10^3$ $\Omega \cdot cm^2$)	4.17	1.92	3.89	1.08	10.67	8.54	10.63	5.18
Q_d ($\times 10^{-5}$ $s^n/\Omega/cm^2$)	31.98	15.87	43.38	44.94	-	-	-	-
n	0.26	1.00	0.26	0.23	-	-	-	-
L ($\times 10^3$ $H \cdot cm^2$)	37.62	51.74	20.25	16.44	-	-	-	-
χ^2 ($\times 10^{-3}$)	3.27	2.70	1.71	11.02	0.80	2.47	0.92	1.29

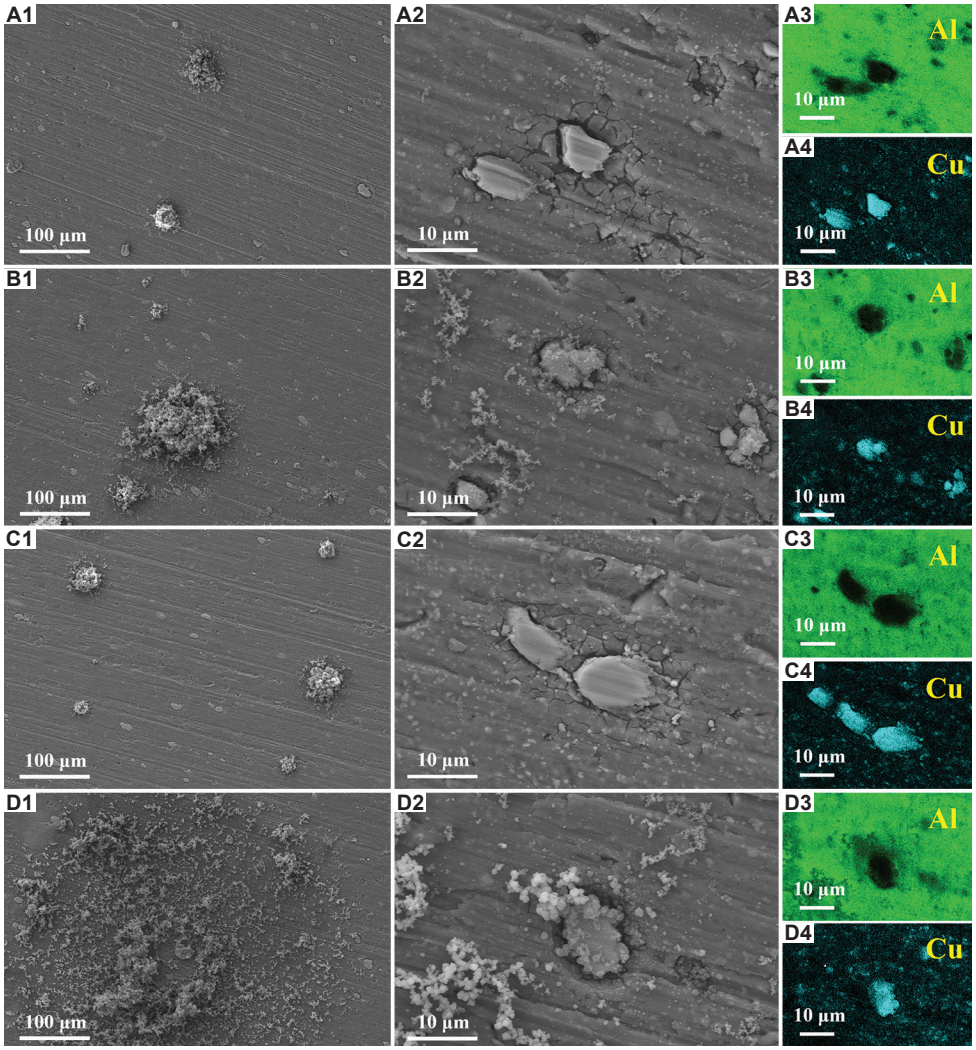

Figure 12. The morphology of the corrosion products and corresponding energy dispersive spectroscopy elemental mapping for the (A_1-A_4) 400-bottom, (B_1-B_4) 400-top, (C_1-C_4) 700-bottom, and (D_1-D_4) 700-top samples after 1 d of exposure to 3.5 wt% NaCl solution. Scale bars: (A_1-D_1) 100 μm; (A_2-D_2, A_3-D_3, A_4-D_4) 10 μm; magnifications: (A_1-D_1) ×200; (A_2-D_2, A_3-D_3, A_4-D_4) ×2000

magnification SEM images further revealed that anodic dissolution of the aluminum matrix preferentially occurred around the Al_2Cu precipitates. Notably, distinct grooves formed by corrosion dissolution were evident around the precipitates on the 400-top and 700-top samples, and the corrosion products were primarily concentrated near these precipitates.

The SEM images of the samples after removal of the corrosion products are presented in Figure 13. The surface of the 400-bottom sample was uniformly covered with small corrosion pits, each measuring <2 μm in size. In contrast, the 700-bottom sample exhibited some pits larger than 10 μm, indicative of more severe corrosion. For the top-layer samples (400-top and 700-top), the sizes of the corrosion pits further increased. The size of the corrosion pits on the surface of the 400-top sample reached nearly 20 μm. The 700-top sample demonstrated the most severe corrosion condition, with the largest corrosion pit areas observed. After extending the immersion time to 7 d, the corrosion state of all four samples significantly deteriorated (Figure 14). Notably, the size of the corrosion pits of the 700-top sample approached 100 μm. Clear evidence of intergranular corrosion was visible in the magnified SEM images. As explained in prior studies, this phenomenon was primarily attributed to fragmented precipitated phase particles distributed predominantly along the grain boundaries, leading to a proliferation of galvanic cells at the grain boundaries. Consequently, the susceptibility to grain boundary attack was significantly enhanced.

The CLSM results for the maximum corrosion pit depth of the four samples are presented in Figure 15. After 1 d of immersion, there were no substantial differences in the

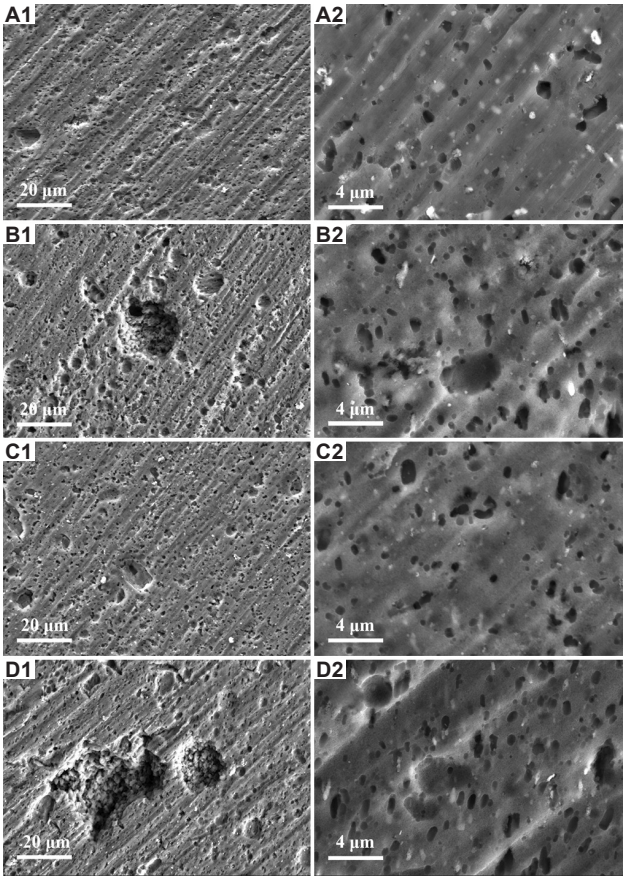

Figure 13. The morphology of corrosion pits developed on the (A_1 and A_2) 400-bottom, (B_1 and B_2) 400-top, (C_1 and C_2) 700-bottom, and (D_1 and D_2) 700-top samples following 1 d of exposure to 3.5 wt% NaCl solution. Scale bars: (A_1-D_1) 20 μm, (A_2-D_2) 4 μm; magnifications: (A_1-D_1) ×1000, (A_2-D_2) ×5000

maximum corrosion pit depth among the four samples, with the 700-top sample exhibiting the highest value of 6.1 μm. After 7 d, the maximum corrosion pit depth on the surface of the 700-top sample increased to 20.1 μm, whereas the 400-bottom sample demonstrated the lowest value, at only 11.7 μm. By integrating the findings from both the corrosion electrochemistry and corrosion morphology tests, it was determined that the bottom-layer samples (400-bottom and 700-bottom) exhibited superior corrosion resistance compared to the top-layer samples (400-top and 700-top), and the corrosion resistance at 400 rpm was more effective than at 700 rpm.

3.5. X-ray photoelectron spectroscopy analysis

To investigate the composition of corrosion products, XPS analysis was performed on the corrosion products from the 400-bottom, 400-top, 700-bottom, and 700-top samples after 1 d of exposure to a 3.5 wt% NaCl solution. The XPS spectra were calibrated using the C 1s peak at a binding energy of 284.8 eV as the reference. Figure 16 displays the high-resolution XPS spectra of Al 2p and O 1s acquired from the corrosion products formed on the four investigated samples. For the Al 2p spectra, three distinct peaks were identified at binding energies of approximately 73.9 eV, 74.6 eV, and 75.5 eV, corresponding to Al_2O_3, $Al(OH)_3$, and $AlCl_3$,[25,54] respectively. Similarly, the deconvolution of the O 1s spectra revealed three component peaks, with binding energies centered at approximately 530.3 eV, 531.7 eV, and 533.0 eV, representing O^{2-} in Al_2O_3, OH^- in $Al(OH)_3$, and adsorbed water (H_2O), respectively.[55] XPS analysis confirmed that Al_2O_3, $Al(OH)_3$, and $AlCl_3$ were the primary components of the corrosion products on all four samples. Furthermore, Table 6 summarizes the peak percentages of the high-resolution Al 2p and O 1s spectra after peak fitting, revealing that $Al(OH)_3$ constituted the largest proportion, while $AlCl_3$ represented the smallest proportion among the detected species.

Due to its small ionic radius (approximately 1.81 Å) and high permeability,[56,57] Cl^- tends to attack the less stable passive film at the interface between the Al_2Cu phase and the surrounding aluminum matrix. Subsequently, Cl^- penetrates the oxide film, reacts with the Al matrix to form soluble aluminum chloride, and then diffuses inward along the AlO(OH) structure. The detailed mechanism is described as follows:[58]

$$AlO(OH) + Cl^- \leftrightarrow AlOCl + OH^- \quad (1)$$

$$AlOCl + OH^- \leftrightarrow AlO(OH) + Cl^- \quad (2)$$

$$Al + Cl^- \leftrightarrow AlCl^{2+} + e^- \quad (3)$$

$$AlCl^{2+} + Cl^- \leftrightarrow AlCl^{2+} + e^- \quad (4)$$

$$AlCl_2 + AlO(OH) \rightarrow AlCl_2(OH) + AlO \quad (5)$$

The proportions of $AlCl_3$ on the surface of the bottom-layer samples (400-bottom and 700-bottom) were smaller compared to those of the top-layer samples (400-top and 700-top), and the proportions of $AlCl_3$ at 400 rpm were lower than at 700 rpm. These findings are in agreement with the results obtained from electrochemical testing and corrosion morphology analysis. Among the samples, the corrosion resistance of the 400-bottom sample was the best.

Based on the observations of the electrochemical behavior and corrosion morphology of the four samples, it can be concluded that there are differences in corrosion resistance both between samples with different rotational speeds and between the top and bottom layers of the as-deposited samples. The primary reason for these differences lies in the varying distributions of precipitated phases on the surfaces of different samples.[59] Numerous studies have demonstrated that precipitates play a crucial role in determining the properties of heat-treatable

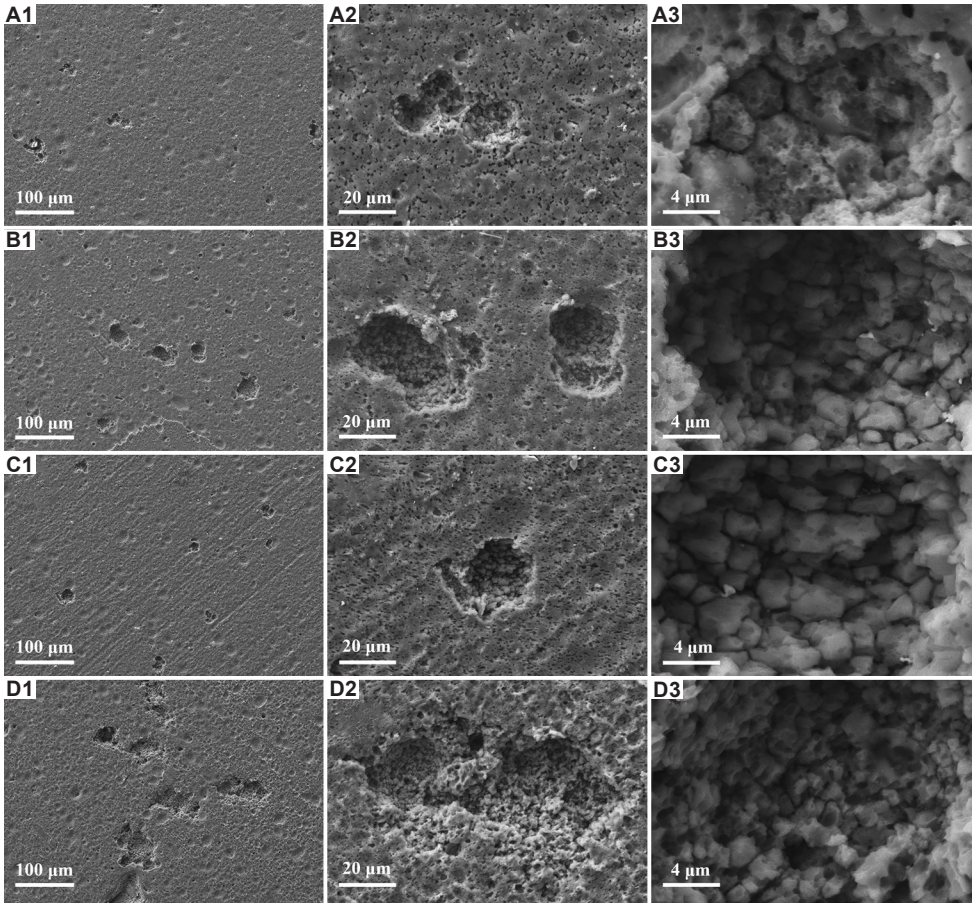

Figure 14. The morphology of corrosion pits developed on the (A_1-A_3) 400-bottom, (B_1-B_3) 400-top, (C_1-C_3) 700-bottom, and (D_1-D_3) 700-top samples following 7 d of exposure to 3.5 wt% NaCl solution. Scale bars: (A_1-D_1) 100 μm, (A_2-D_2) 20 μm, (A_3-D_3) 4 μm; magnifications: (A_1-D_1) ×200, (A_2-D_2) ×1000, (A_3-D_3) ×5000

Table 6. Percentage proportions of each deconvoluted peak in high-resolution X-ray photoelectron spectroscopy spectra of Al 2p and O 1s

Samples	Al 2p (%)			O 1s (%)		
	Al_2O_3	Al $(OH)_3$	$AlCl_3$	O^{2-} (OX)	OH^-	O^{2-} (H_2O)
400-bottom	39.84	50.80	9.36	13.40	70.03	16.57
400-top	35.37	45.33	19.30	13.64	72.01	14.35
700-bottom	33.81	52.77	13.42	14.98	69.90	15.12
700-top	35.24	42.87	21.89	15.53	65.13	19.34

aluminum alloys.[60,61] In our previous study,[25] it was confirmed that the Al_2Cu precipitate exhibits cathodic characteristics relative to the matrix, and the aluminum matrix surrounding the precipitate is more susceptible to pitting corrosion. This is consistent with the viewpoint in other studies that the matrix adjacent to Cu-containing metallic compounds is more prone to pitting.[62-64] After pitting corrosion is initiated by the galvanic couple, the accumulation of metal cations in the corrosion product layer attracts Cl^- to gradually diffuse into the alloy.[65] In addition, since Al_2Cu tends to distribute at grain boundaries,[66] it further induces intergranular corrosion. Therefore, the distribution of precipitates plays a crucial role in the corrosion behavior of alloys.

Samples in the bottom layer of the as-deposited structure, having undergone more thermal cycles than those in the top layer, were exposed to high temperatures for a longer duration. This led to more Al_2Cu particles re-dissolving into the aluminum matrix to form a supersaturated solid solution, ultimately resulting in a lower coverage of precipitated phases and fewer micro-galvanic couples in the bottom layer compared to the top layer (Figure 3). In addition, the bottom layer exhibited a higher degree of recrystallization and a relatively lower dislocation density within the grains (Figure 8), reducing the number of pitting initiation sites. Furthermore, during the DRX of AFSD, a larger grain size was formed in the bottom layer (Figure 6), which decreased the grain boundary density and thereby

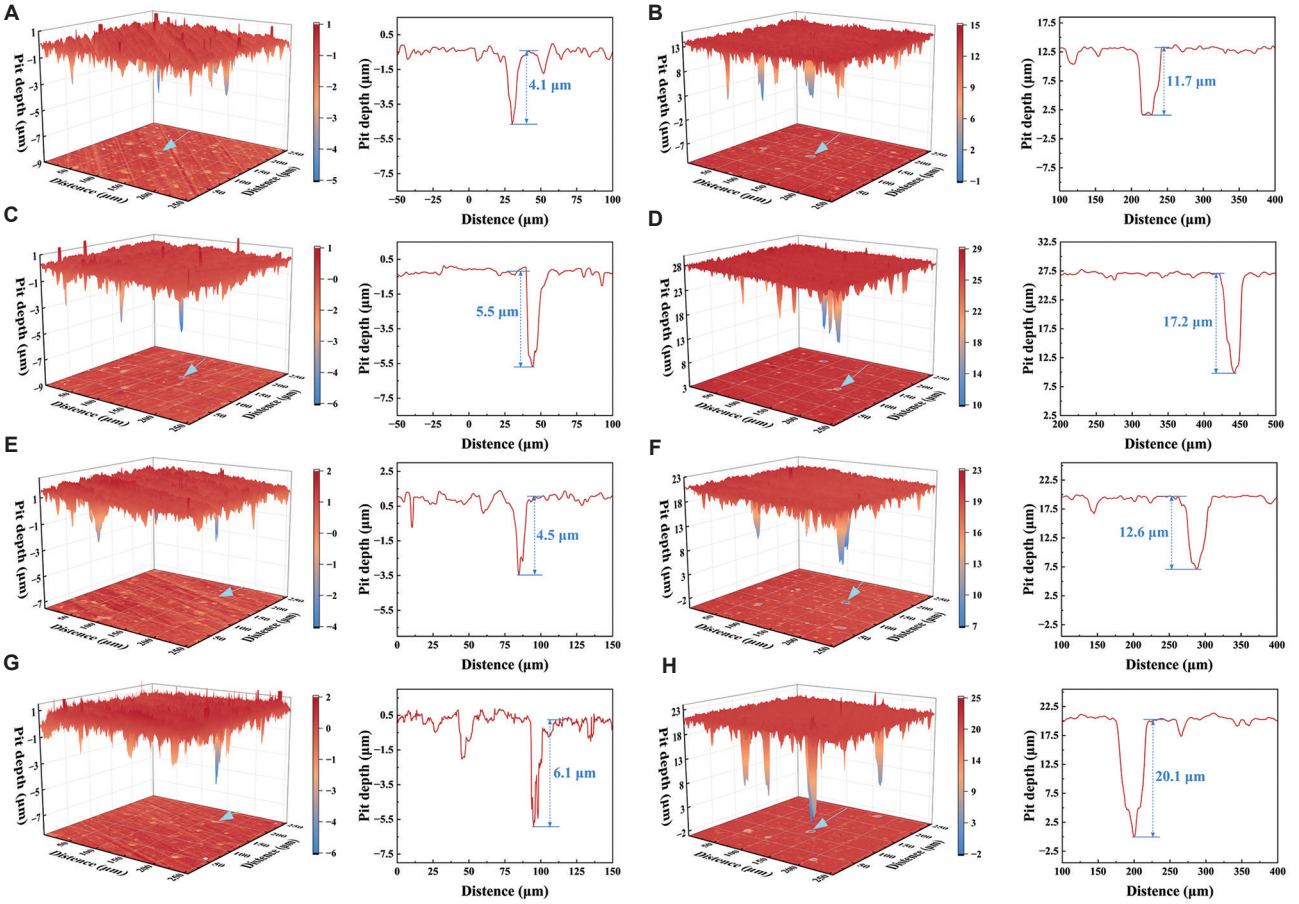

Figure 15. Confocal laser scanning microscopy images and the maximum pit depth for the (A and B) 400-bottom, (C and D) 400-top, (E and F) 700-bottom, and (G and H) 700-top samples following (A, C, E, G) 1 d and (B, D, F, H) 7 d of exposure to 3.5 wt% NaCl solution

Table 7. Summary of key result data for this work

Material	Rotational speed (rpm)	Spindle temperature (°C)	F_{spi} (kN)	Grain size (μm)	GOS (°)	R_{ct} ($\times 10^3\ \Omega \cdot cm^2$)
400-bottom	400	460.64±27.89	6.91±1.64	3.40	2.54	4.17
400-top	400	460.64±27.89	6.91±1.64	2.50	4.26	1.92
700-bottom	700	503.27±33.94	8.03±1.69	3.83	2.08	3.89
700-top	700	503.27±33.94	8.03±1.69	3.01	3.19	1.08

Abbreviation: GOS: Grain orientation spread.

reduced the paths for intergranular corrosion. These factors collectively contributed to the stronger corrosion resistance of the bottom layer.

Compared to the 400 rpm samples, the 700 rpm samples showed a higher degree of recrystallization (Figure 8) and larger grain size (Figure 6). These results are consistent with the findings in relevant studies that grain size shows a positive correlation with rotational speed.[27,28,67] This, to some extent, inhibits the initiation and propagation of corrosion. However, the higher temperature generated at 700 rpm prolonged the cooling time, during which more Al_2Cu particles precipitated (Figure 3). This increased the number of weak sites on the aluminum alloy surface and the quantity of micro-galvanic couples, thereby reducing corrosion resistance. EIS plots (Figure 10) and corrosion morphology images (Figures 13 and 14) revealed that the 400 rpm specimens exhibited superior corrosion performance compared to the 700 rpm ones, indicating that precipitated phases exert a more significant influence on corrosion resistance.

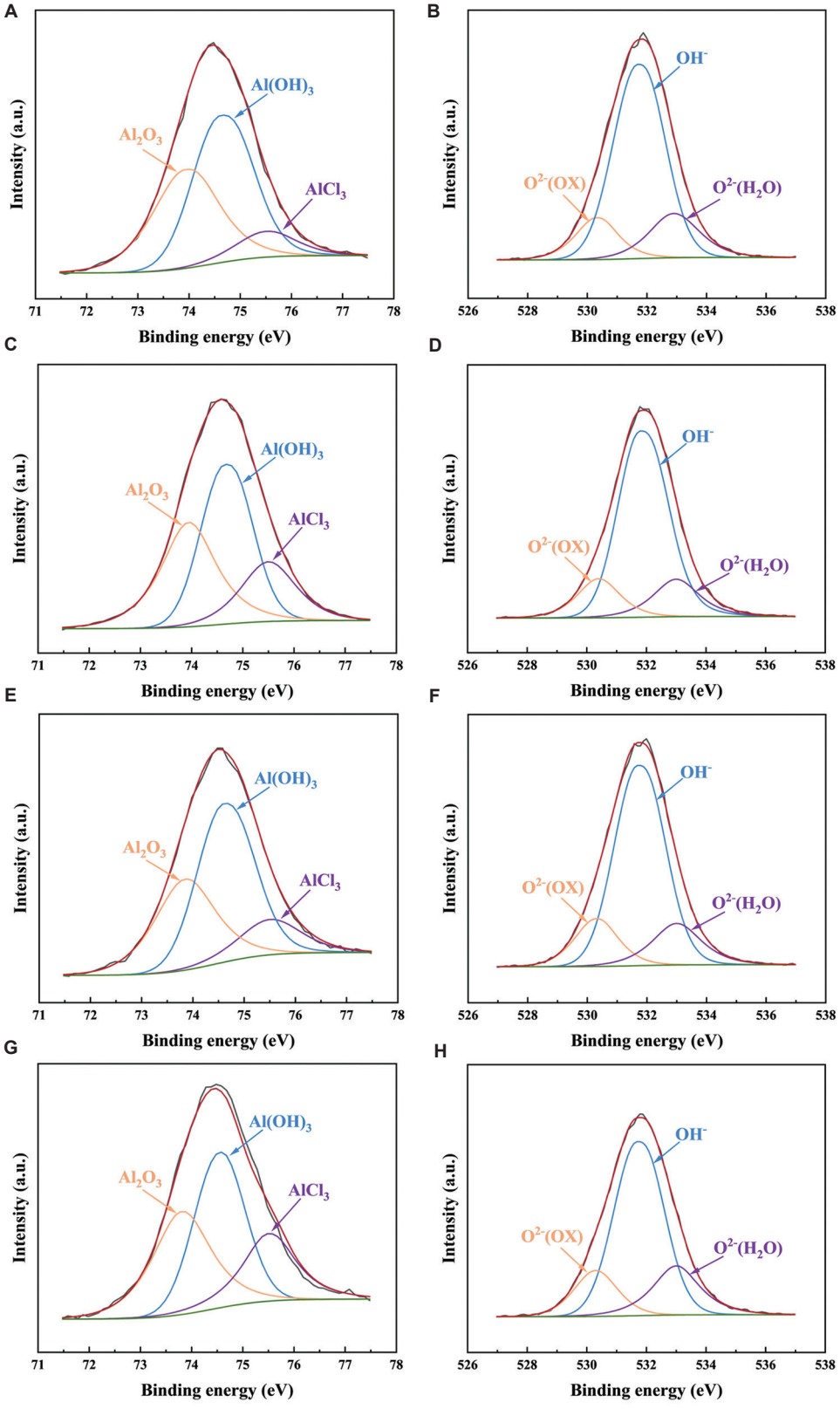

Figure 16. The high-resolution X-ray photoelectron spectroscopy spectra of (A, C, E, G) Al 2p and (B, D, F, H) O 1s acquired from the corrosion products of the (A and B) 400-bottom, (C and D) 400-top, (E and F) 700-bottom, and (G and H) 700-top samples

The key test results of this work are summarized in Table 7. It can be concluded that the 400-bottom sample, despite being processed under lower spindle rotational speed, spindle temperature, and F_{spi}, exhibits the best corrosion resistance. This provides insights for fabricating large-scale corrosion-resistant components. However, the variation in corrosion resistance at different heights of the as-deposited component poses a critical limiting factor for the preparation of such corrosion-resistant structures. Addressing this issue may require the establishment of a constant-temperature environment or the application of post-processing heat treatments. Furthermore, based on this work, future research should focus on integrating artificial intelligence to develop a predictive model for the relationship between AFSD process parameters, microstructure, and properties, enabling the reverse design of alloy components according to specific requirements.

4. Conclusion

In this study, 2219 aluminum alloys were fabricated via the AFSD method under different rotational speeds. This work focused on the systematic analysis of the microstructure and corrosion behavior of top-layer and bottom-layer samples extracted from as-deposited aluminum alloys at different rotational speeds. The principal findings can be summarized as follows:

i. Compared to 400 rpm, the rotational speed of 700 rpm resulted in higher heat input and more pronounced plastic deformation, both of which promoted the recrystallization process. At the bottom layer of the as-deposited alloy, the grain size and the proportion of HAGBs increased from 3.40 μm to 3.83 μm and from 71.5% to 75.2%, respectively, when the rotational speed was raised from 400 rpm to 700 rpm. At the top region of the as-deposited alloy, the grain size and the fraction of HAGBs increased from 2.50 μm to 3.01 μm and from 57.3% to 63.0%, respectively, under the same change in rotational speed.

ii. At 400 rpm, there were fewer Al_2Cu phases on the alloy surface than at 700 rpm. This reduced the number of Al_2Cu phase/aluminum matrix galvanic couples on the alloy surface. Compared to 700 rpm, the R_{ct} values of the bottom and top layers of the as-deposited alloy at 400 rpm were 4.17×10^3 Ω·cm^2 (vs. 3.89×10^3 Ω·cm^2 [700 rpm]) and 1.92×10^3 Ω·cm^2 (vs. 1.08×10^3 Ω·cm^2 [700 rpm]), respectively. These results indicate that the lower rotational speed contributes to an improvement in corrosion resistance.

iii. For the AFSD-2219 aluminum alloys at both 400 rpm and 700 rpm, the bottom layer underwent more multi-layer thermal cycling effects than the top layer. Therefore, the bottom layer exhibited a higher degree of recrystallization and fewer Al_2Cu phases, thus showing superior corrosion resistance compared to the top layer.

Acknowledgments

None.

Funding

This work was supported by the National Key R&D Program of China (2023YFE0205300), the Guangdong Basic and Applied Basic Research Foundation (2021B1515130009), and the Fundamental Research Funds for the Central Universities (FRF-BD-25-044), and the National Natural Science Foundation of China (No. 52201062).

Conflicts of interest

Qian Qiao, Dawei Guo, and Lap Mou Tam are employees of IDQ Science and Technology Development (Hengqin, Guangdong) Co., Ltd., while Zhixiong Zhu and Yongyong Lin are employees of Aerospace Engineering Equipment (Suzhou) Co., Ltd.; however, they were not involved in any activities that could constitute a conflict of interest in relation to this study. Other authors declare that they have no known competing financial interests or personal relationships that could have appeared to influence the work reported in this paper.

Authors' contributions

Conceptualization: Hongchang Qian, Zikang Wang
Data curation: Zikang Wang
Formal analysis: Min Zhou
Funding acquisition: Dawei Zhang
Investigation: Zikang Wang, Zhixiong Zhu, Yongyong Lin
Methodology: Chi Tat Kwok
Project administration: Dawei Guo
Resources: Dawei Guo, Dawei Zhang
Software: Min Zhou
Supervision: Hongchang Qian, Dawei Guo, Dawei Zhang, Lap Mou Tam
Visualization: Qian Qiao
Writing – original draft: Zikang Wang
Writing – review & editing: Hongchang Qian, Qian Qiao

Ethics approval and consent to participate

Not applicable.

Consent for publication

Not applicable.

Availability of data

The data that support the findings of this study are available from the corresponding author on reasonable request.

References

1. Ghalandari MA, Mirsalehi SE, Kiani S. Production of nanocomposite parts using AA6061-T6 consumable rods via friction stir method: A novel approach of solid-state additive manufacturing of CNT-reinforced aluminum matrix nanocomposites. *Mater Today Commun*. 2025;42:111435.

   doi: 10.1016/j.mtcomm.2024.111435

2. Sahraei A, Mirsalehi SE. An investigation on application of friction stir additive manufacturing (FSAM) for the production of AA6061/TiC-graphene hybrid nanocomposite in the shape of multi-layer cylindrical part. *J Mater Res Technol*. 2024;30:6737-6752.

   doi: 10.1016/j.jmrt.2024.05.043

3. Li F, Zhang W, Kooi BJ, Pei Y. Eutectic aluminum alloys fabricated by additive manufacturing: A comprehensive review. *J Mater Sci Technol*. 2026;250:123-164.

   doi: 10.1016/j.jmst.2025.06.016

4. Tao H, Cai Q, Chen M, Zhang W, Cao G, Zhang H. Effect of heat treatment on the microstructure and corrosion performance of 2219 Al alloy cold sprayed coatings. *Corros Sci*. 2024;241:112526.

   doi: 10.1016/j.corsci.2024.112526

5. He H, Yi Y, Huang S, Zhang Y. An improved process for grain refinement of large 2219 Al alloy rings and its influence on mechanical properties. *J Mater Sci Technol*. 2019;35:55-63.

   doi: 10.1016/j.jmst.2018.09.007

6. Han F, Li C, Wang Y, *et al*. Comparative study on corrosion property of 2219 aluminum alloy sheet and additively manufactured 2319 aluminum alloy. *J Mater Res Technol*. 2024;30:3178-3785.

   doi: 10.1016/j.jmrt.2024.04.036

7. Grilli R, Baker MA, Castle JE, Dunn B, Watts JF. Localized corrosion of a 2219 aluminium alloy exposed to a 3.5% NaCl solution. *Corros Sci*. 2010;52:2855-2866.

   doi: 10.1016/j.corsci.2010.04.035

8. Mao X, Yi Y, He H, Huang S, Guo W. Second phase particles and mechanical properties of 2219 aluminum alloys processed by an improved ring manufacturing process. *Mater Sci Eng A*. 2020;781:139226.

   doi: 10.1016/j.msea.2020.139226

9. Qiao Q, Gong X, Guo D, *et al*. Influence of tool head geometry on *in situ* monitoring of temperature, force, and torque during additive friction deposition of aluminum alloy 2219. *Mater Sci Addit Manuf*. 2025;4:025280060.

   doi: 10.36922/MSAM025280060

10. Chang W, Gao J, Qian H, *et al*. Microbiologically influenced corrosion of friction-surfaced 630 stainless steel coating in the presence of *Pseudomonas aeruginosa*. *Corros Sci*. 2025;245:112708.

    doi: 10.1016/j.corsci.2025.112708

11. Zhao Y, Jin Z, Xu B, *et al*. Effect of surface cleaning on interface bonding performance for 316H stainless steel joints manufactured by additive forging. *Mater Des*. 2021;210:110025.

    doi: 10.1016/j.matdes.2021.110025

12. Qiao Q, Zhou M, Gong X, *et al*. *In-situ* monitoring of additive friction stir deposition of AA6061: Effect of layer thickness on the microstructure and mechanical properties. *Addit Manuf*. 2024;84:104141.

    doi: 10.1016/j.addma.2024.104141

13. Deng R, Wei R, Liang J, *et al*. Microstructure and wear characteristics of austenitic stainless steel coatings fabricated through various directed energy deposition. *Mater Sci Addit Manuf*. 2024;3:4974.

    doi: 10.36922/msam.4974

14. Marchal V, Zhang Y, Labed N, Lachat R, Peyraut F. Fast layer fiber orientation optimization method for continuous fiber-reinforced material extrusion process. *Mater Sci Addit Manuf*. 2023;2:49.

    doi: 10.36922/msam.49

15. Petram R, Wisdom C, Montelione A, *et al*. On the surface integrity resulting from laser powder bed fusion of Ti6Al4V: Improvements by cavitation abrasive surface finishing. *Mater Sci Addit Manuf*. 2025;5:025280062.

    doi: 10.36922/MSAM025280062

16. Korgancı M, Bozkurt Y. Recent developments in additive friction stir deposition (AFSD). *J Mater Res Technol*. 2024;30:4572-4583.

    doi: 10.1016/j.jmrt.2024.04.179

17. Tuncer N, Bose A. Solid-state metal additive manufacturing: A review. *JOM*. 2020;72:3090-3111.

    doi: 10.1007/s11837-020-04260-y

18. Khodabakhshi F, Gerlich AP. Potentials and strategies of solid-state additive friction-stir manufacturing technology: A critical review. *J Manuf Processes*. 2018;36:77-92.

    doi: 10.1016/j.jmapro.2018.09.030

19. Shao J, Samaei A, Xue T, *et al*. Additive friction stir deposition of metallic materials: Process, structure and properties. *Mater Des*. 2023;234:112356.

    doi: 10.1016/j.matdes.2023.112356

20. Yasa E, Poyraz O, Molyneux A, Sharman A, Bilgin GM, Hughes J. Systematic review on additive friction stir deposition: Materials, processes, monitoring and modelling. *Inventions*. 2024;9:116.

    doi: 10.3390/inventions9060116

21. Khan AS. *Advanced Solid-State Dissimilar Material Joining and Additive Manufacturing for Enabling Multi-Material Lightweight Structures. Thesis*; 2024.

doi: 10.7302/23746

22. Anderson-Wedge K, Avery DZ, Daniewicz SR, *et al*. Characterization of the fatigue behavior of additive friction stir-deposition AA2219. *Int J Fatigue*. 2021;142:105951.

doi: 10.1016/j.ijfatigue.2020.105951

23. Zhang M, Ye X, Li Y, Wang H, Lai R, Li Y. Effect of heat treatment states of feedstock on the microstructure and mechanical properties of AA2219 layers deposited by additive friction stir deposition. *Materials*. 2023;16:7591.

doi: 10.3390/ma16247591

24. Rivera OG, Allison PG, Brewer LN, *et al*. Influence of texture and grain refinement on the mechanical behavior of AA2219 fabricated by high shear solid state material deposition. *Mater Sci Eng A*. 2018;724:547-558.

doi: 10.1016/j.msea.2018.03.088

25. Wang Z, Qian H, Chang W, *et al*. Microstructure and localized corrosion properties of 2219 aluminum alloy manufactured by additive friction stir deposition. *Corros Sci*. 2024;240:112508.

doi: 10.1016/j.corsci.2024.112508

26. Elshaghoul YGY, El-Sayed Seleman MM, Bakkar A, *et al*. Additive friction stir deposition of AA7075-T6 alloy: Impact of process parameters on the microstructures and properties of the continuously deposited multilayered parts. *Appl Sci*. 2023;13:10255.

doi: 10.3390/app131810255

27. Qiao Q, Wang L, Tam CW, *et al*. *In-situ* monitoring of additive friction stir deposition of AA6061: Effect of rotation speed on the microstructure and mechanical properties. *Mater Sci Eng A*. 2024;902:146620.

doi: 10.1016/j.msea.2024.146620

28. Chen G, Wu K, Wang Y, Zhu Z, Nie P, Hu F. Effect of rotational speed and feed rate on microstructure and mechanical properties of 6061 aluminum alloy manufactured by additive friction stir deposition. *Int J Adv Manuf Technol*. 2023;127:1165-1176.

doi: 10.1007/s00170-023-11527-6.

29. Prabhakar DAP, Shettigar AK, Herbert MA, *et al*. A comprehensive review of friction stir techniques in structural materials and alloys: Challenges and trends. *J Mater Res Technol*. 2022;20:3025-3060.

doi: 10.1016/j.jmrt.2022.08.034

30. Qiao Q, Tam CW, Lam WI, *et al*. Hybrid heat-source solid-state additive manufacturing: A method to fabricate high performance AA6061 deposition. *J Mater Sci Technol*. 2025;228:107-124.

doi: 10.1016/j.jmst.2024.11.079

31. Garcia D. *Investigation of the Processing History During Additive Friction Stir Deposition Using in-Process Monitoring Techniques*. Doctoral Dissertations. Virginia Tech; 2021. Available from: https://hdl.handle.net/10919/111376

32. Ambrosio D, Wagner V, Dessein G, Vivas J, Cahuc O. Machine learning tools for flow-related defects detection in friction stir welding. *J Manuf Sci Eng*. 2023;145:101005.

doi: 10.1115/1.4062457

33. Bourgeois L, Zhang Y, Zhang Z, Chen Y, Medhekar NV. Transforming solid-state precipitates via excess vacancies. *Nat Commun*. 2020;11:1248.

doi: 10.1038/s41467-020-15087-1

34. Krasnikov VS, Mayer AE, Pogorelko VV, Gazizov MR. Influence of θ' phase cutting on precipitate hardening of Al-Cu alloy during prolonged plastic deformation: Molecular dynamics and continuum modeling. *Appl Sci*. 2021;11:4906.

doi: 10.3390/app11114906

35. Straumal BB, Kulagin R, Klinger L, *et al*. Structure refinement and fragmentation of precipitates under severe plastic deformation: A review. *Materials (Basel)*. 2022;15:601.

doi: 10.3390/ma15020601

36. Xu D, Jiang M, Meng L, Zhu M, Liu Y, Zhang X. Interfacial characteristics, interfacial oxide evolution and bonding mechanism of 2219 aluminum alloy joints manufactured by hot-compression bonding. *J Mater Res Technol*. 2024;30:3036-3051.

doi: 10.1016/j.jmrt.2024.04.080

37. Tang W, Yang X, Tian C, Xu Y. Interfacial grain structure, texture and tensile behavior of multilayer deformation-based additively manufactured Al 6061 alloy. *Mater Charact*. 2023;196:112646.

doi: 10.1016/j.matchar.2023.112646

38. Li H, Lin J, Dean TA, Wen SW, Bannister AC. Modelling mechanical property recovery of a linepipe steel in annealing process. *Int J Plast*. 2009;25:1049-1065.

doi: 10.1016/j.ijplas.2008.09.001

39. Rizi MS, Minouei H, Lee BJ, Pouraliakbar H, Toroghinejad MR, Hong SI. Data supporting the hierarchically activated deformation mechanisms to form ultra-fine grain microstructure in carbon containing FeMnCoCr twinning induced plasticity high entropy alloy. *Data Brief*. 2022;42:108052.

doi: 10.1016/j.dib.2022.108052

40. Pouraliakbar H, Howells A, Gallerneault M, Fallah V. Fracture behavior of a rapidly solidified thin-strip continuous cast AA5182 Al-Mg alloy with the Portevin-Le Chatelier effect under varying strain rates. *J Alloys Compd*.

2024;971:172810.

doi: 10.1016/j.jallcom.2023.172810

41. Doherty RD. The deformed state and nucleation of recrystallization. *Met Sci*. 1974;8:132-142.

doi: 10.1179/msc.1974.8.1.132

42. Hadadzadeh A, Mokdad F, Wells MA, Chen DL. A new grain orientation spread approach to analyze the dynamic recrystallization behavior of a cast-homogenized Mg-Zn-Zr alloy using electron backscattered diffraction. *Mater Sci Eng A*. 2018;709:285-289.

doi: 10.1016/j.msea.2017.10.062

43. Ayad A, Allain-Bonasso N, Rouag N, Wagner F. Grain orientation spread values in if steels after plastic deformation and recrystallization. *Mater Sci Forum*. 2012;702-703:269-272.

doi: 10.4028/www.scientific.net/MSF.702-703.269

44. Sprouster DJ, Streit Cunningham W, Halada GP, *et al*. Dislocation microstructure and its influence on corrosion behavior in laser additively manufactured 316L stainless steel. *Addit Manuf*. 2021;47:102263.

doi: 10.1016/j.addma.2021.102263

45. Chang W, Wang X, Qian H, *et al*. Effect of Sn addition on microstructure, hardness and corrosion behavior of CoCrFeNiSnx high entropy alloys in chloride environment. *Corros Sci*. 2024;227:111808.

doi: 10.1016/j.corsci.2023.111808

46. Lou Y, Chang W, Cui T, Qian H, Hao X, Zhang D. Microbiologically influenced corrosion inhibition induced by *S. putriefaciens* mineralization under extracellular polymeric substance regulation via *FlrA* and *FlhG* genes. *Corros Sci*. 2023;221:111350.

doi: 10.1016/j.corsci.2023.111350

47. Zhang HH, Liu YW, Bian H, *et al*. Electrodeposition of silane/reduced graphene oxide nanocomposite on AA2024-T3 alloy with enhanced corrosion protection, chemical and mechanical stability. *J Alloys Compd*. 2022;911:165058.

doi: 10.1016/j.jallcom.2022.165058

48. Ameer MA, Fekry AM, Heakal FET. Electrochemical behaviour of passive films on molybdenum-containing austenitic stainless steels in aqueous solutions. *Electrochim Acta*. 2004;50:43-49.

doi: 10.1016/j.electacta.2004.07.011

49. Jorcin JB, Orazem ME, Pébère N, Tribollet B. CPE analysis by local electrochemical impedance spectroscopy. *Electrochim Acta*. 2006;51:1473-1479.

doi: 10.1016/j.electacta.2005.02.128

50. Cui T, Qian H, Chang W, *et al*. Towards understanding *Shewanella algae*-induced degradation of passive film of stainless steel based on electrochemical, XPS and multi-mode AFM analyses. *Corros Sci*. 2023;218:111174.

doi: 10.1016/j.corsci.2023.111174

51. Zhao L, Qian H, Chang W, *et al*. Effect of aging heat treatment on microbiologically influenced corrosion of 17-4PH stainless steel by *Pseudomonas aeruginosa*. *Corros Sci*. 2024;227:111739.

doi: 10.1016/j.corsci.2023.111739

52. Shoar Abouzari MR, Berkemeier F, Schmitz G, Wilmer D. On the physical interpretation of constant phase elements. *Solid State Ionics*. 2009;180:922-927.

doi: 10.1016/j.ssi.2009.04.002

53. Huang Y, Shih H, Mansfeld F. Concerning the use of constant phase elements (CPEs) in the analysis of impedance data. *Mater Corros*. 2010;61:302-305.

doi: 10.1002/maco.200905385

54. Wang B, Zhang L, Su Y, Mou X, Xiao Y, Liu J. Investigation on the corrosion behavior of aluminum alloys 3A21 and 7A09 in chloride aqueous solution. *Mater Des*. 2013;50:15-21.

doi: 10.1016/j.matdes.2013.02.080

55. Babu AP, Choudhary S, Griffith JC, Huang A, Birbilis N. On the corrosion of a high solute Al-Zn-Mg alloy produced by laser powder bed fusion. *Corros Sci*. 2021;189:109626.

doi: 10.1016/j.corsci.2021.109626

56. McCafferty E. Sequence of steps in the pitting of aluminum by chloride ions. *Corros Sci*. 2003;45:1421-1438.

doi: 10.1016/S0010-938X(02)00231-7

57. Li P, Du M. Effect of chloride ion content on pitting corrosion of dispersion-strengthened-high-strength steel. *Corros Commun*. 2022;7:23-34.

doi: 10.1016/j.corcom.2022.03.005

58. Bockris JO, Minevski LV. On the mechanism of the passivity of aluminum and aluminum alloys. *J Electroanal Chem*. 1993;349:375-414.

doi: 10.1016/0022-0728(93)80186-L

59. Abbasi-Nahr M, Mirsalehi SE. Additive friction stir deposition of AA5083/MoS2-diamond hybrid nanocomposites: Investigating their metallurgical, mechanical, tribological, and electrochemical characteristics, and process-structure-property relationships. *J Alloys Compd*. 2025;1013:178553.

doi: 10.1016/j.jallcom.2025.178553

60. Kiani S, Mirsalehi SE. Friction stir additive manufacturing of B4C and graphene reinforced aluminum matrix hybrid nanocomposites using consumable pins. *J Mater Res Technol*. 2024;28:1094-1110.

doi: 10.1016/j.jmrt.2023.12.065

61. Kiani S, Mirsalehi SE, Sahraei A. Linear and cylindrical

friction stir additive manufacturing (FSAM) of AA6061-T6 by consumable rods: Metallurgical structure, wear, and corrosion properties. *Weld World*. 2024;68:2869-2889.

doi: 10.1007/s40194-024-01839-w

62. Obispo HM, Murr LE, Arrowood RM, Trillo EA. Copper deposition during the corrosion of aluminum alloy 2024 in sodium chloride solutions. *J Mater Sci*. 2000;35:3479-3495.

doi: 10.1023/A:1004840908494

63. Na KH, Pyun SI. Comparison of susceptibility to pitting corrosion of AA2024-T4, AA7075-T651 and AA7475-T761 aluminium alloys in neutral chloride solutions using electrochemical noise analysis. *Corros Sci*. 2008;50:248-258.

doi: 10.1016/j.corsci.2007.05.028

64. Suter T, Alkire RC. Microelectrochemical studies of pit initiation at single inclusions in Al 2024-T3. *J Electrochem Soc*. 2001;148:B36.

doi: 10.1149/1.1344530

65. Xu W, Liu J. Microstructure and pitting corrosion of friction stir welded joints in 2219-O aluminum alloy thick plate. *Corros Sci*. 2009;51:2743-2751.

doi: 10.1016/j.corsci.2009.07.004

66. Koteswara Rao SR, Madhusudhan Reddy G, Srinivasa Rao K, Kamaraj M, Prasad Rao K. Reasons for superior mechanical and corrosion properties of 2219 aluminum alloy electron beam welds. *Mater Charact*. 2005;55:345-354.

doi: 10.1016/j.matchar.2005.07.006

67. Zhu X, Wang R, Wang L, Liu M, Li S. Effect of rotational shear and heat input on the microstructure and mechanical properties of large-diameter 6061 aluminium alloy additive friction stir deposition. *Crystals*. 2024;14:581.

doi: 10.3390/cryst14070581